



Pushing the boundaries  
of chemistry?  
It takes  
#HumanChemistry

Make your curiosity and talent as a chemist matter to the world with a specialty chemicals leader. Together, we combine cutting-edge science with engineering expertise to create solutions that answer real-world problems. Find out how our approach to technology creates more opportunities for growth, and see what chemistry can do for you at:

[evonik.com/career](https://www.evonik.com/career)



# Single Crystals Heterogeneity Impacts the Intrinsic and Extrinsic Properties of Metal–Organic Frameworks

Adrian Fuchs, Petra Mannhardt, Patrick Hirschle, Haoze Wang, Irina Zaytseva, Zhe Ji, Omar Yaghi, Stefan Wuttke,\* and Evelyn Ploetz\*

At present, an enormous characterization gap exists between the study of the crystal structure of a material and its bulk properties. Individual particles falling within this gap cannot be fully characterized in a correlative manner by current methods. The authors address this problem by exploiting the noninvasive nature of optical microscopy and spectroscopy for the correlative analysis of metal-organic framework particles *in situ*. They probe the intrinsic as well as extrinsic properties in a correlated manner. The authors show that the crystal shape of MIL-88A strongly impacts its optical absorption. Furthermore, the question of how homogeneously water is distributed and adsorbed within one of the most promising materials for harvesting water from humid air, MOF-801, is addressed. The results demonstrate the considerable importance of the particle level and how it can affect the property of the material.

over, they are often invasive,<sup>[2]</sup> require high vacuum,<sup>[3]</sup> or preclude real-space information,<sup>[4]</sup> thus preventing *in situ* studies of materials. These two characterization levels are also reflected in current research efforts, for instance, on metal–organic frameworks (MOFs) that mainly focus on two distinct aspects: molecular structures being tuned and bulk properties being measured.<sup>[5]</sup> MOF chemists often vary the molecular building units (e.g., installation of a functional group) and examine the corresponding change in the performance of a bulk sample (e.g., gas adsorption isotherm). Alteration of MOF particle properties can be caused twofold: (1) by differences in “extrinsic properties”, that is, physical parameters


## 1. Introduction

An ongoing challenge in material science is to determine whether the bulk properties are represented by the individual particles. The difficulty arises because most common characterization methods measure statistical averages over an entire sample to achieve an enhanced signal-to-noise ratio. While high-resolution imaging or diffraction techniques can access the single-particle level, they are unsuited for multiple-particle screening and often probe only one aspect of a sample.<sup>[1]</sup> More-

like their particle size, shape, and surface structure, or (2) by variations in “intrinsic properties” ruled by chemical attributes of the framework. These include casual differences in the composition of building blocks,<sup>[6]</sup> crystallinity,<sup>[7]</sup> functionalization,<sup>[8]</sup> and defects,<sup>[2]</sup> but also designed variations as in multivariate MOFs. The interplay of both kinds of properties determines the overall performance for any application; the mutual impact of intrinsic and extrinsic variations correlated to any change in individual particle properties *in situ* is challenging to explore in a correlative manner.

A. Fuchs, P. Mannhardt, P. Hirschle, I. Zaytseva, S. Wuttke, E. Ploetz  
Department of Chemistry and Center for NanoScience (CeNS)  
LMU Munich  
81377 Munich, Germany  
E-mail: stefan.wuttke@bcmaterials.net; evelyn.ploetz@lmu.de

H. Wang, Z. Ji, O. Yaghi  
Department of Chemistry  
University of California–Berkeley  
Materials Sciences Division  
Lawrence Berkeley National Laboratory  
Kavli Energy NanoSciences Institute at Berkeley  
and Berkeley Global Science Institute  
Berkeley, CA 94720, USA

 The ORCID identification number(s) for the author(s) of this article can be found under <https://doi.org/10.1002/adma.202104530>.

© 2021 The Authors. Advanced Materials published by Wiley-VCH GmbH. This is an open access article under the terms of the Creative Commons Attribution License, which permits use, distribution and reproduction in any medium, provided the original work is properly cited.

Z. Ji  
Department of Chemistry, Stanford University  
Stanford, CA 94305, USA

O. Yaghi  
UC Berkeley-KACST Joint Center of Excellence for Nanomaterials for Clean Energy Applications  
King Abdulaziz City for Science and Technology  
Riyadh 11442, Saudi Arabia

S. Wuttke  
BCMmaterials  
Basque Center for Materials  
UPV/EHU Science Park  
Leioa 48940, Spain

S. Wuttke  
Ikerbasque  
Basque Foundation for Science  
Bilbao 48013, Spain

DOI: 10.1002/adma.202104530

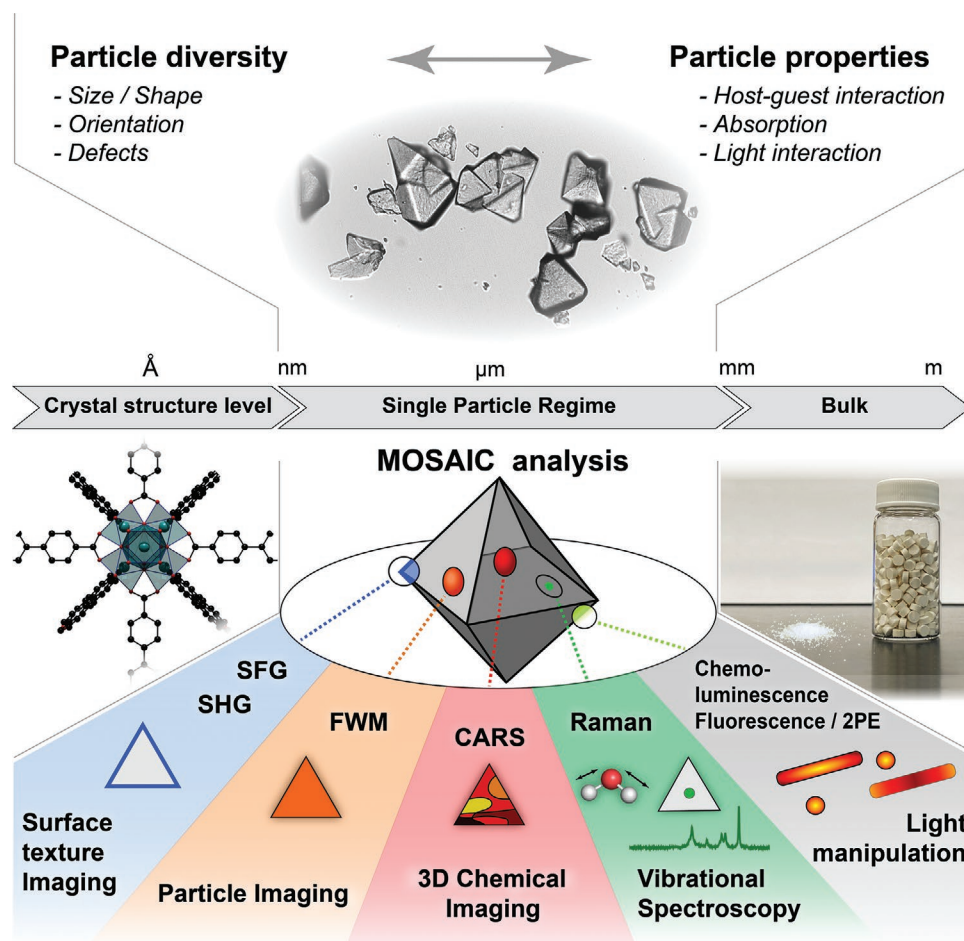


**Figure 1.** Graphic illustration of the MOSAIC analysis for the single-particle level characterization. The lower colored panels provide an overview of available MOSAIC methods, the observed particle characteristics, and the general modality behind the method. Images from left to right: crystal structure, brightfield image, and crystalline powder of MOF UiO-67. Abbreviations: SFG: sum-frequency generation; SHG: second harmonic generation; FWM: four-wave-mixing; CARS: coherent anti-Stokes Raman scattering; 2PE: two-photon excitation.

Optical microscopy has proven to be a reliable approach for the characterization of MOF particles, beyond bulk experiments.<sup>[9–11]</sup> Fluorescence microscopy, which relies on light-emitting functional groups or molecules as readout, could reveal key properties and parameters of MOFs by studying the location, distribution, and interplay of luminescent probes with the hosting MOF scaffold.<sup>[9]</sup> Even the level of defects and heterogeneity within MOFs could be probed at the nano level with advanced fluorescence lifetime methods.<sup>[10,12]</sup> Label-free methods, including nonlinear microscopy,<sup>[13,14]</sup> and vibrational, microspectroscopic tools<sup>[15]</sup> based on Raman scattering or IR absorption, have demonstrated their strength by following guest molecules in MOFs across micrometer-sized crystals while probing the surrounding environment and defect distributions.

Here, we report the development of a dedicated multifunctional imaging system to monitor in situ how spatial variations and particle diversity influence the material properties of MOFs without the need to consecutively use separate methodologies. We combined space-resolved fluorescence and Raman spectroscopy with a suite of optical confocal imaging techniques, which we abbreviate as multimodal optical spectroscopy and

in situ imaging correlating (MOSAIC) approach (**Figure 1**). The designed MOSAIC platform combines five modalities for correlative material characterization: (1) second harmonic generation (SHG) and sum-frequency generation (SFG) to visualize the surface texture of MOF crystals; (2) the electronic response generated by four-wave-mixing (FWM) to investigate particle morphology and heterogeneity; (3) polarization-sensitive coherent anti-Stokes Raman scattering (pCARS) for mapping the 3D distribution of chemical compounds within the reticular frameworks; (4) space-resolved vibrational spectroscopy, that is, spontaneous Raman scattering, to identify and quantify any changes within the modified host material; (5) two-photon-induced chemiluminescence as a reporter signal for direct targeting light-sensitive materials. All five modalities for imaging and spectroscopy are complementary to each other and extendable by modalities that provide, for example, higher spatial resolution or faster data acquisition.<sup>[16]</sup>

The power of the label-free MOSAIC platform was demonstrated first on the multimodal characterization of single crystals of UiO-67, an archetypical MOF, as a proof-of-concept. Next, we turned our attention toward probing MOFs' extrinsic properties (i.e., particle-dependent interactions with light).

Specifically, we investigated the photochemical behaviors of the MOF, MIL-88A, which can serve as nano-antennas and exhibit morphology-dependent responses. The micron-sized crystals resonate shape-dependently with incident laser irradiation, allowing for a selective, optically triggered manipulation of crystals. Finally, we examined the intrinsic property (guest–framework interaction) of water adsorption in MOF-801 and found that water adsorbs in clusters within the material, which is characterized by missing cluster defects. Thus, the label-free, multimodal platform developed here enables us to reveal the impact of crystal heterogeneities in MOFs.

## 2. Results and Discussion

### 2.1. Development of Multimodal Imaging and Spectroscopy

The developed multimodal setup is shown in Figure 2a (Experimental Section, Note S1, Supporting Information) and based on a confocal laser-scanning microscope (CLSM) with two types of laser sources: (1) we implemented continuous wave (CW) lasers in the visible for fluorescence and spontaneous Raman scattering-based imaging and spectroscopy; and (2) we incorporated an all-fiber-based, jitter-free, dual-color femtosecond-laser in the near-infrared (NIR) for nonlinear imaging. The excitation laser at 774 nm was implemented as the pump laser, while the laser excitation at 1053 nm served for super-continuum generation between 770 and 1100 nm in a photonic crystal fiber (Note S1, Supporting Information). Both NIR light sources (and their combinations) are dedicated to probing nonlinear optical responses in MOF crystals at the confocal volume. The nonlinear responses are detected by avalanche photodiodes (APD) and recorded via a dual-channel time-correlated single-photon counting (TCSPC) card. Spectral information originating from the confocal volume is collected in epi-direction by a spectrograph equipped with an emCCD camera. The sCMOS camera is implemented as the third detection alternative in epi-direction and used for bright-field imaging to position the sample on the confocal microscope.

The spectroscopic signatures of the imaging modalities are designed to occur between 390 and 750 nm (Figure 2b). They are orthogonally combinable and, hence, allow for probing different material properties simultaneously. Here, label-free processes are based on nonlinear interactions of the pulsed laser fields with the investigated material and are described by their higher-order, nonlinear susceptibility  $\chi^{(n)}$ . The expected power dependencies for each spectroscopic signature were experimentally confirmed (Note S2 and Figure S1, Supporting Information). A detailed overview of each method is given in Table S1, Supporting Information.

To characterize metal–organic framework particles spectroscopically in a label-free manner, we incorporated SHG and SFG (Figure 2c) using the fundamental laser lines at 774 and 1053 nm of the dual-color fs-laser. The observed signals (Figure 2b) were generated at  $\omega_{\text{SHG}} = 2 \cdot \omega_{\text{pump}}$  and  $\omega_{\text{SFG}} = \omega_{\text{pump}} + \omega_{\text{probe}}$  and observed at 387 and 457.8 nm, respectively. To probe the inner structure and chemical composition of MOF particles, we incorporated FWM and CARS imaging in the red to NIR spectral range. FWM occurs at  $\omega_{\text{FWM}} = 2 \omega_{\text{pump}} - \omega_{\text{probe}}$  (Figure 2c), that is, its spectral signature is blue-shifted

with respect to the pump pulse at 774 nm. In this paper, we mainly use FWM at 612 nm, if not stated otherwise. To provide chemical sensitivity, we chose the wavelength of the probe pulse  $\omega_{\text{probe}}$ , such that the energy difference between both light fields  $\omega_{\text{pump}} - \omega_{\text{probe}}$  coincides with a specific vibrational transition  $\omega_i$  of the material; in Figure 2b, it is illustrated for the C–C stretch vibration in UiO-67 at 688 nm, that is, at  $1614 \text{ cm}^{-1}$ . This resonantly enhanced FWM process is referred to as CARS (Figure 2c). To suppress any additional, non-resonant, electronic background, we exploited the polarization-dependence of the signal and implemented polarization-sensitive CARS (pCARS; Experimental Section).<sup>[17]</sup> In combination with spectral focusing,<sup>[18]</sup> we established pCARS as a fast 3D chemical imaging tool that selectively maps characteristic Raman resonances of MOFs. As the last imaging contrast, we incorporated one-photon (1PE) and two-photon excitation (2PE) induced fluorescence imaging at 532 and 774 nm (Figure 2c). These allowed mainly for addressing fluorescent probes or MOF materials emitting in the blue/green spectral range (Figure 2b) if combined with other modalities probed by our MOSAIC approach.

Next, we demonstrated the strength of the MOSAIC platform to correlatively image and spectrally characterize reticular materials, in particular, MOF at the single-particle level. In a proof-of-concept experiment, we studied the electronic and vibrational properties of UiO-67 particles (Note S4, Supporting Information) in a space-resolved manner. To probe the surface properties of unlabeled UiO-67 particles, we used both spectroscopic signatures: SHG and SFG. SHG allows for the mapping of surfaces or non-centrosymmetric materials and polarization information in crystalline structures (Table S1, Supporting Information). SFG as a second-order nonlinear optical response is equally sensitive to non-centrosymmetric species as it is usually the case for symmetry-breaking interfaces. As seen in both panels of Figure 2d, both types of imaging clearly show the surface roughness of UiO-67 and reveal cracks and substructures of the particle surface, which are barely visible in bright-field images. Next, we tested two label-free imaging modalities to access the 3D structure of UiO-67, namely FWM and pCARS (Figure 2e,f). The spectral regions addressed for FWM (no spectral resonance) and pCARS (resonant to the strong peak at  $1615 \text{ cm}^{-1}$ ) are marked in Figure 2g. The particles show a very homogeneous signature and regular shape identical to the bright-field image, as it is expected from the crystalline, solid material with little to no defects. FWM and pCARS offer strong 2D sectioning capabilities that restrict the detected signal to single cross-sections through the UiO-67 assembly. Consecutively, it can reconstruct the inner structure of MOF crystals in 3D (Figure S2, Supporting Information). To control the homogeneous chemical composition of UiO-67, we further employed spontaneous Raman spectroscopy within the particle volume as well as at air–particle interfaces of the same particle in addition to CARS microscopy. (Figure S3, Supporting Information). A detailed assignment of vibrations in the solid-state Raman spectra of linker and UiO-67 (Figure 2g) is given in Table S2, Supporting Information. In line with space-resolved Raman mapping of the sample (Figure S4, Supporting Information), both measurements yielded no spectral differences in the recorded Raman signatures but concomitantly confirmed the crystallinity of the sample (Figure S5, Supporting Information).

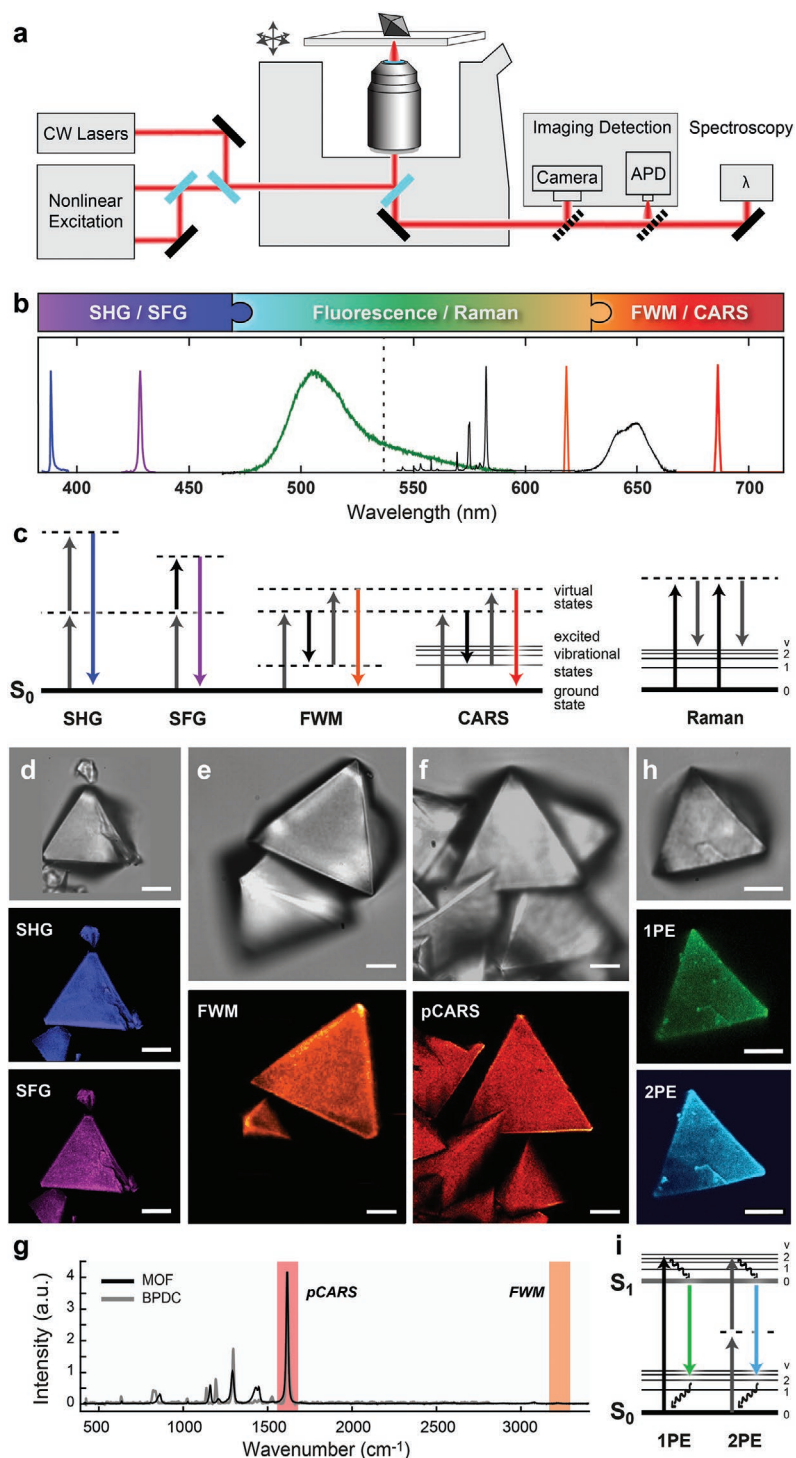


**Figure 2.** MOSAIC analysis: physical background, technical realization, and characterization of UiO-67 crystals. a) Schematic of the multimodal, scanning microscope. b) Incorporated imaging modalities are spectrally complementary: SHG and SFG occurs at 387 and 458 nm as shown on a silica wafer; 2PE induced emission of RBITC is centered around 510 nm; Raman scattering in UiO-67 and water after 532 nm excitation can be detected between 550 and 650 nm and FWM and pCARS in UiO-67 for example, at 612 and 688 nm. c) Energy diagrams of the implemented nonlinear processes, including SHG, SFG, FWM, CARS, and Stokes Raman scattering. d–f) Unlabeled UiO-67 particles imaged by bright field and nonlinear microscopy, including SHG and SFG (d), FWM at  $3300\text{ cm}^{-1}$  ( $616\text{ nm}$ ); e), and pCARS at  $1615\text{ cm}^{-1}$  ( $688.2\text{ nm}$ ); f), g) Spontaneous Raman signature of UiO-67 particles and their linker molecule BPDC in solid state phase. The spectral regions chosen for FWM and pCARS imaging in panel (e,f) are marked in red and orange, respectively. h) Brightfield and fluorescence images of RBITC-labeled particles after 1PE and 2PE induced emission at 532 and 774 nm. i) Corresponding energy diagrams for 1PE and 2PE induced fluorescence in panel (h). Scale bars:  $10\text{ }\mu\text{m}$ . Arrows indicate the electric fields of exciting light sources and resulting signatures.

To highlight the flexibility of the developed system, we further incorporated luminescence-based imaging with a high signal-to-noise ratio. Figure 2h shows fluorescently labeled UiO-67 particles after one-photon excitation (1PE, green; Figure 2i) at 532 nm and two-photon excitation (2PE, cyan; Figure 2i) at 774 nm. These particles were labeled with 2-RhodamineB-isothiocyanate (RBITC) at the particle surface based on a linker-exchange reaction,<sup>[10]</sup> while particles in Figure 2d–f were completely unlabeled. Due to the 1.6-fold better axial resolution as well as the centrosymmetric sensitivity of 2PE imaging, small cracks and defects at the surface are more visible. Nevertheless, intrinsic labeling of 3D structures is challenging and interferes with the original particle structure. Labeling alters the material under investigation. Moreover, the fluorescence emission is inherently spectrally broad (Figure 2b), which significantly limits the multiplexing capabilities. Overall, the one- and two-photon excitation images in Figure 2h highlight the resolution enhancement of nonlinear optical microscopy compared to one-photon CLSM. The developed multimodal microscope system can combine these modalities orthogonally, as demonstrated for simultaneous 2PE, SHG, and FWM imaging (Figure S6, Supporting Information).

## 2.2. Correlating MIL-88A Crystal Morphologies with Their Optical Properties

To illustrate the influence of extrinsic properties of MOF crystals, we investigate the correlation between the optical properties and different morphologies of MIL-88A via our MOSAIC platform. We draw our attention to MIL-88A since it is frequently employed for applications including drug delivery,<sup>[19]</sup> sensing,<sup>[20]</sup> and photocatalysis,<sup>[21]</sup> but also synthesized in a large variety of different morphologies.<sup>[22]</sup> We exploited the label-free modalities of our microscope in combination with spatially resolved spectroscopy since the quenching behavior of the iron centers in MIL-88A renders fluorescence-based single-particle studies challenging.

MIL-88A crystals can be synthesized in four different distinct morphologies:<sup>[22]</sup> as needle-like and bipyramidal microparticles with sizes of  $\approx 1\text{--}4\ \mu\text{m}$ , bipyramidal nanoparticles with diameters  $\approx 300\text{--}500\ \text{nm}$ , and spherical nanoparticles of 50 nm in size (Note S4, Supporting Information). Independent of their morphology, all particle types show an identical unit cell as seen from the XRD.<sup>[22]</sup> Similar findings were made using Raman spectroscopy (Figure S7, Supporting Information). While the Raman signature of linker molecules strongly differs from MIL-88A particles, it is remarkably similar for particles with different morphologies (Table S3, Supporting Information). No additional enhancement effects or shifts in Raman resonances due to varying particle geometries were observed. To study the influence of extrinsic properties on the optical properties of MOF crystals, we chose crystalline microparticles, which differ in morphology but share similar dimensions. Figure 3a,b shows the SEM images of both microparticle morphologies. We first determined the length and width distribution for both morphologies by label-free FWM imaging at  $\approx 3400\ \text{cm}^{-1}$  (i.e., at 612.7 nm; Figure 3c; Figure S8, Supporting Information). The elongated needle-shaped particles have a length of  $3.29\ (\pm 1.12)$

$\mu\text{m}$  and a width of  $0.79\ (\pm 0.34)\ \mu\text{m}$ . The broad length distribution with an FWHM of  $2.52\ \mu\text{m}$  can be explained by the unsynchronized stochastic growth during synthesis.

In contrast, the approximately spherical, bipyramidal microparticles show a narrow distribution  $1.47\ (\pm 0.23)\ \mu\text{m}$  in length and  $1.26\ (\pm 0.18)\ \mu\text{m}$  in width. Next, we imaged a mixture of both morphologies with FWM microscopy to study how this spatial variance of the MIL-88A morphologies influences their electronic response. While both types of particles are sensitive to FWM (Figure 3d, upper panels), the observed FWM intensity of MIL-88A needles depends on two parameters: the volume of individual particles and the alignment with respect to the *p*-polarization of the excitation laser field. Horizontally aligned particles are maximally susceptible to FWM. Their observed intensity decreases with an increasing angle toward the horizontal orientation. It almost vanishes for particles with a vertical alignment as seen in the upper panels of Figure 3d. In contrast, bipyramids are strongly susceptible to FWM without any preferred orientation. In addition to FWM, they surprisingly exhibit chemiluminescence (CL; Figure 3d, blue, lower right panel) with a spectrally broad emission spectrum, easily distinguishable from the FWM response (Figure S9, Supporting Information). This property is not observed for needle-shaped MIL-88A particles at an identical excitation power (i.e., below 1.9 and 0.1 mW for the pump and probe laser pulses). The observed luminescence is accompanied by a strongly progressing degradation and consecutive splitting of particles (Figure 3d, left lower panel, marked particle). The degradation products are visible in the bright-field channel. They co-localize with the bipyramidal particles before the scanning and the detected CL signature during the imaging process.

Degradation and resulting chemiluminescence of the MIL-88A microcrystals can occur, when the absorbed energy provided by the pulsed, incident laser radiation is higher than the activation energy for the oxidation reaction with surrounding oxygen (Figure S9c, Supporting Information). Here, the optical absorption of (sub-)micron-sized particles is not only dependent on the absorption coefficient of the material itself, but also on morphology-dependent resonances, so-called Mie modes.<sup>[23]</sup> Their contribution to absorption and scattering of light by small particles becomes most dominant when the light-induced electromagnetic field inside the particle boundaries becomes resonant with the incident light fields. As predicted for elongated particles,<sup>[24]</sup> the absorption of micron-sized particles is dictated by their chemical composition, the incident laser field, the surrounding medium as well as their size and shape. Since the first conditions are identical for the different types of MIL-88A microcrystals, differences in absorption behavior are thought to only depend on the shape or size of the crystals (or both). As shown in Figure 3b, which highlights the major axis (length) and the minor axis (width) for needle and bipyramidal crystals, the overall shapes of the particles mainly differ in the width over length ratio. We, hence, introduced the ellipticity per particle as a ratiometric parameter to describe their morphology. It is given as 1 minus the width to length ratio and varies between 0 and 1 for spherical and elongated particles, respectively. The advisability of the ellipticity parameter is illustrated when comparing the volumes of needle-like and bipyramidal particles, which can be approximately

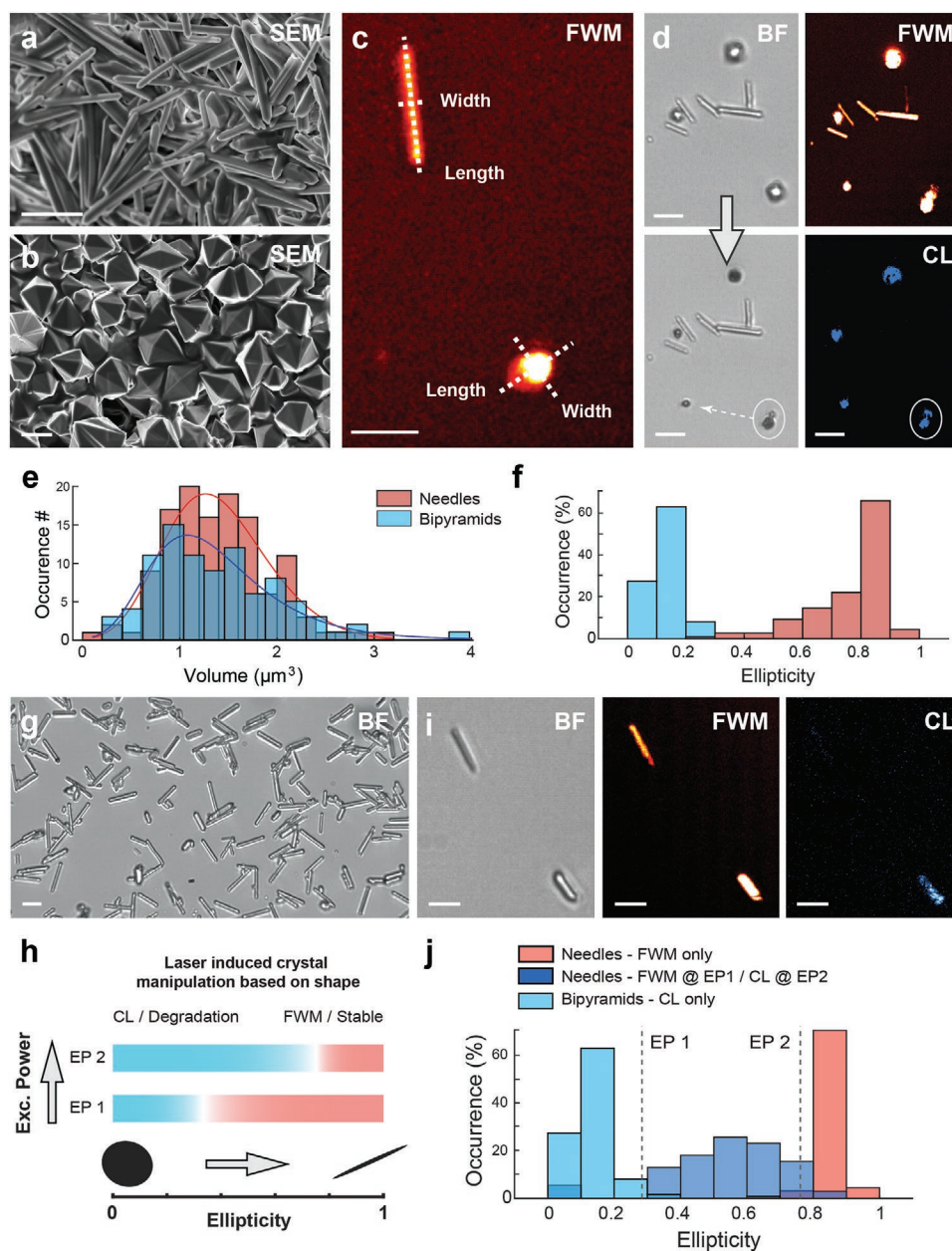


**Figure 3.** Optical behavior of MIL-88A crystals for different morphologies. a,b) SEM images of particles in needle (a) and bipyramidal morphology (b). c) Label-free FWM imaging at  $3400\text{ cm}^{-1}$  can determine length and width for every particle. d) Correlative imaging by brightfield, chemiluminescence (CL), and four-wave-mixing FWM. e) The volume and f) ellipticity distributions for each morphology clarify the difference in optical behavior. While both morphologies are comparable in volume (Needles:  $V = 1.08 \pm 0.52\ \mu\text{m}^3$ ;  $N = 246$ . Bipyramids:  $V = 1.18 \pm 0.49\ \mu\text{m}^3$ ;  $N = 115$ ), they are distinguishable by their ellipticity (Needles:  $E = 0.81 \pm 0.09$ ;  $N = 246$  / Bipyramids:  $E = 0.13 \pm 0.04$ ;  $N = 115$ ). g) The wide distribution in ellipticity represents the variance in particle length of needle-like MIL-88A, also observed in brightfield. h) Schematic of the observed correlation between CL occurrence and ellipticity depending on the excitation power from panel (f) at  $EP_1 = 1.9\text{ mW}$ . An increased excitation power ( $EP_2 = 3.0\text{ mW}$ ) is expected to shift the absorption threshold to higher ellipticities, resulting in increased CL for needle-like particles. i) BF, FWM, and CL images of needle-shaped crystals at  $EP_2$ . Only the bipyramidal particle shows CL. Scale bars:  $1\ \mu\text{m}$ . j) Ellipticity distribution of needles showing only FWM (red,  $N = 75$ ), needles showing CL at  $EP_2$  (lilac,  $N = 40$ ), and bipyramidal particles (light blue,  $N = 115$ ). The dashed lines indicate roughly the threshold for the respective excitation powers. Scale bar (except panel (i)):  $2\ \mu\text{m}$ .

described as ellipsoidal and spherical volume. Their distribution is depicted in Figure 3e,f (Note S5, Supporting Information). While the needle-like particles feature a slightly larger volume of  $1.08 (\pm 0.52)\ \mu\text{m}^3$  than bipyramids ( $1.18 \pm 0.49\ \mu\text{m}^3$ ) on average, they still share a similar distribution (Figure S8 and

Table S4, Supporting Information). The overlap of both distributions is very high, dissuading the idea that size is the dominant factor for intrinsic particle absorption. It is further supported by the fact that bipyramidal crystals of varying sizes show chemiluminescence due to degradation, while needles of similar

volume stay intact (Figure S10, Supporting Information). The ellipticity, on the other hand, clearly differentiates between the morphologies and varies between 0.81 ( $\pm 0.09$ ) for needles and 0.13 ( $\pm 0.04$ ) in the case of bipyramids. Notably, the ellipticity distribution of the bipyramids is narrow, while the distribution of needle-like particles features a sharp peak around 0.85 and a broad width between 0.3 and 0.8.

Overall, needle-like particles show a wide distribution in size and shape (Figure 3g). As indicated by the additional chemiluminescence (Figure 3d), there might be a strong correlation between the reduced ellipticity of particles and the enhanced interaction of the exciting laser field. Our results predict that more sphere-like particles with small ellipticity foster the coupling of the exciting laser field to the particle and consecutively, the emission of chemiluminescence by single MIL-88A crystals (Figure 3h). This implies we could generate chemiluminescence in needle-like particles by adjusting the incident excitation power and target MIL-88A crystals below a certain ellipticity threshold specifically. The observed FWM signature of MIL-88A results from a nonlinear interaction with two pulses laser sources: a spectrally broad but chirped probe beam at low intensity and a spectrally narrow pump beam at high intensities. While we used an excitation power of  $I_{\text{probe}} = 0.1$  mW and  $I_{\text{pump}} = 1.9$  mW at first (Figure 3c–f; which we referred to as excitation power  $EP_1$ ), we increased the excitation power of the pump beam to 3.0 mW ( $EP_2$ ) to test our hypothesis in the following. When measuring particles with needle morphology at higher excitation power, we, indeed, found the same variance in absorption behavior for the particles as in the artificial mixture of needle and bipyramidal morphologies depicted in Figure 3c. One fraction was susceptible to FWM only, while other particles showed additional chemiluminescence (Figure 3i). To exclude the possibility that the luminescent particles have a different chemical composition, we additionally used single-particle-based spontaneous Raman spectroscopy (Figure S11, Supporting Information). The spectrum clearly identified the luminescent particle as MIL-88A. When sorting the ellipticities of individual needle particles according to their absorption behavior, we could directly distinguish between the “FWM only” fraction and the luminescent fraction (Figure 3j). The group of particles only featuring an FWM signal as the optical response was characterized by a narrow distribution (FWHM = 0.07) of elongated needles centered with an ellipticity of  $\approx 0.86$  ( $\pm 0.015$ ). The degraded particles (CL, lilac) featured a much broader distribution (FWHM = 0.33), centered around 0.63 ( $\pm 0.07$ ). They comprise a mixture of particles with varying degrees of the needle and the bipyramidal morphology. The dashed grey lines in Figure 3j indicate the ellipticity threshold for the optical absorption at the two different excitation power levels. Of additional interest in ellipticity is the overlap of both fractions between 0.7 and 0.9. The existence of this group of particles can be explained by two scenarios, in which the intrinsic optoelectronic properties of well-defined needle particles are altered: (1) it depends on a coupling of magnetic fields by neighboring particles, similar to the reported behavior of dielectric silica rods.<sup>[25]</sup> This is dependent on the proximity and concentration of particles and should vanish for not-stationary particles in solution. Indeed, we found such

enhanced light-induced degradation of MOF needles for overlapping MIL-88A particles (Figure S12a, Supporting Information). (2) The absorption is caused by an increase in the morphologic complexity as suggested by Kulachenkov et al.<sup>[26]</sup> Our findings indicate that the observed absorption might be the result of defects within the MOF structure (Figure S12b, Supporting Information). Hence, MOSAIC enabled us to unveil the relationship between the extrinsic property of particle morphology with their absorption behavior. To further highlight the impact of local variances on intrinsic properties, we investigated the water distribution in MOF-801 crystals.

### 2.3. Particle-Dependent Host–Guest Interactions of MOF-801

MOF-801 is an auspicious material for harvesting water from humid air.<sup>[27]</sup> It was reported that MOF-801 single crystals with lower volume have a higher affinity to water than larger-sized particles.<sup>[28]</sup> This difference, however, could not be explained by the crystal size alone nor correlated with the local morphology and intrinsic properties of the material. We, hence, investigated the position-dependent performance of water adsorption in MOF-801 particles in situ.

MOF-801 crystals feature an octahedral shape with sizes up to tenths of micrometers with triangular faces. They consist of zirconium oxide clusters and fumaric acid linkers arranged in a cubic framework (Note S4, Supporting Information).<sup>[28]</sup> Per unit cell, three water binding sites are reported: two tetrahedral and one octahedral binding site. Starting from the dry MOF material, water molecules attach first to primary binding sites, that is, the zirconium oxide clusters in the tetrahedral cavities. Consecutively, water molecules bridge the primarily bound molecules in the tetrahedral cavities before filling up the octahedral cavities until saturation is reached.<sup>[28]</sup> To elucidate the distribution of water in MOF-801, we employed Raman spectroscopy and hyperspectral imaging in combination with pCARS imaging, next. **Figure 4a** depicts the Raman spectrum of the evacuated MOF-801 (black curve). The MOF scaffold is characterized by its dominant bands at  $\approx 1440$   $\text{cm}^{-1}$  (symmetric O–C–O stretching mode),  $\approx 1666$   $\text{cm}^{-1}$  (C–C stretching mode), and  $\approx 3150$   $\text{cm}^{-1}$  (C–H stretch vibration) and is in excellent agreement with the literature (Table S5, Supporting Information). The stretch mode of  $\mu_3$ –OH in Zr cluster is present as a sharp resonance at 3680  $\text{cm}^{-1}$  (Figure 4b). Upon exposure to humid air, additional water molecules diffuse into the material and adsorb within the pores. This process alters the Raman spectrum, most dominantly between 3100 and 3700  $\text{cm}^{-1}$  (Figure 4a,b): the signature of the hydroxyl groups in the crystal lattice around 3680  $\text{cm}^{-1}$  vanishes due to hydrogen bonding with adsorbed water molecules while a broad Raman resonance between 3200 and 3600  $\text{cm}^{-1}$  appears due to the O–H stretch vibration of bridging water molecules (spectra at  $\approx 33\%$  RH). This broad peak is characteristic for liquid water and served to visualize the water adsorption in the framework via Raman based imaging.

We, therefore, addressed the question of how homogeneously water is distributed and adsorbed within MOF-801. To map the water distribution over a region of interest and



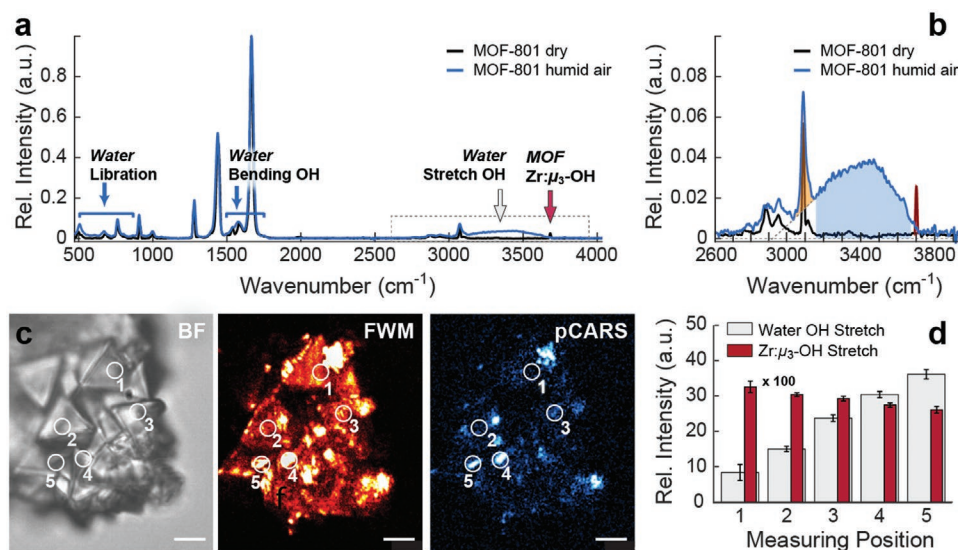


**Figure 4.** Water adsorption in MOF-801. a) Raman spectrum of MOF-801 in dry (black) and humid environment (blue; 32%RH). Characteristic spectral contributions due to adsorbed water and the hydroxyl vibration within the Zr cluster are marked with arrows. b) Zoom-in of (a). The integrated bands serve to determine the relative amount of water and hydrogen bonding compared to MOF-801. c) Water distribution in MOF-801 crystals visualized by brightfield, FWM, and pCARS imaging at 10%RH. Numbered circles indicate measurement points in (d). Scale bar: 2  $\mu\text{m}$ . d) Relative amount of adsorbed water observed by Raman spectroscopy at selected areas in panel (b).

quantify the absolute amount of water at 3%RH, we employed spatially-resolved pCARS imaging in addition to brightfield and FWM imaging. Figure 4c displays an example area of clustered crystals at 22.1  $^{\circ}\text{C}$  and 3%RH. While brightfield and FWM imaging showed a random clustering of crystals, the pCARS modality revealed an additional, surprisingly uneven distribution of water molecules over the field of view. Most areas showed a similar level of uptaken water as observed by hyperspectral Raman imaging on homogeneously grown crystals (Figure S13, Supporting Information), but small, localized spots exhibited a significantly higher water content. We performed in situ Raman spectroscopy at selected points in the region of interest to exclude the possibility that this distribution could be an artifact introduced by the imaging modality or a potential nonlinear FWM background hampering a quantitative determination of uptaken water. Using the linear concentration dependence of spontaneous Raman scattering, we determined the relative amount of water compared to MOF-801 (Figure 4c; Note S6, Supporting Information) and found a correlation between an increased level of adsorbed water and the increase in pCARS intensity (Figure 4d). Concomitantly, we observe a reduction in signal strength of the  $\mu_3$ -OH stretch in Zr cluster around 3680  $\text{cm}^{-1}$ , which can be ascribed to the formation of hydrogen bonds between adsorbed water molecules and the  $\mu_3$ -H residue. Although less prominent, we equally observe localized water accumulations in samples exposed to higher humidity (Figure S14, Supporting Information). Water molecules tend to accumulate in small, confined areas (e.g., at measuring position 5, Figure 4c). When comparing the results from brightfield and pCARS imaging of various particles in 3D, we could indeed identify locally confined volumes with enhanced, incorporated water (Figure S15, Supporting Information) that co-localized with deformed crystals visible in the brightfield channel.

Structural defects are ubiquitous and occur at various levels in MOFs,<sup>[29]</sup> starting at missing linkers and/or metal sites, substitutional defects over to crystal mismatches or amorphous particles, to name a few. In particular, extended defects in MOF, that is, at a grain boundary of two crystals or within polycrystalline areas, could contribute to the enhanced water uptake. To decipher the underlying mechanism of water collection and the chemical nature of the observed defects, we set out for various correlative approaches. We combined pCARS imaging for fast chemical identification, spontaneous Raman spectroscopy to probe the local chemical fingerprint of the material and/or the defects, fluorescence imaging for monitoring local cluster defects and FWM imaging, which allows to visualize structural defects<sup>[14]</sup> by probing the electronic response of the material.

Enhanced water incorporation is spatially confined in 3D as observed by pCARS (Figure 5a). FWM imaging can identify spatial inhomogeneities (as seen at locations 1–3), which frequently (but not conclusively) coincide with areas localized by pCARS. Confined water uptake below the dew point can only occur if additional space due to missing linker or metal sites is available. To answer the question, if enhanced FWM signals were due to unsaturated metal sites, we made use of the liquid-phase, acid-catalyzed self-condensation reaction<sup>[30]</sup> of furfuryl alcohol (FA). Oligomerization of the colorless FA takes place at accessible Brønsted acid sites leading to fluorescent products (see Note S7, Supporting Information). We employed two-photon excited fluorescence microscopy in correlation with FWM imaging to probe the spatial distribution of the FA condensation mediated by MOF-801 via fluorescence imaging and the material's response by FWM (Figure 5b,c). As expected, we observed pronounced emission in the green channel (520–600 nm), at uneven surfaces and cracks (white area), as

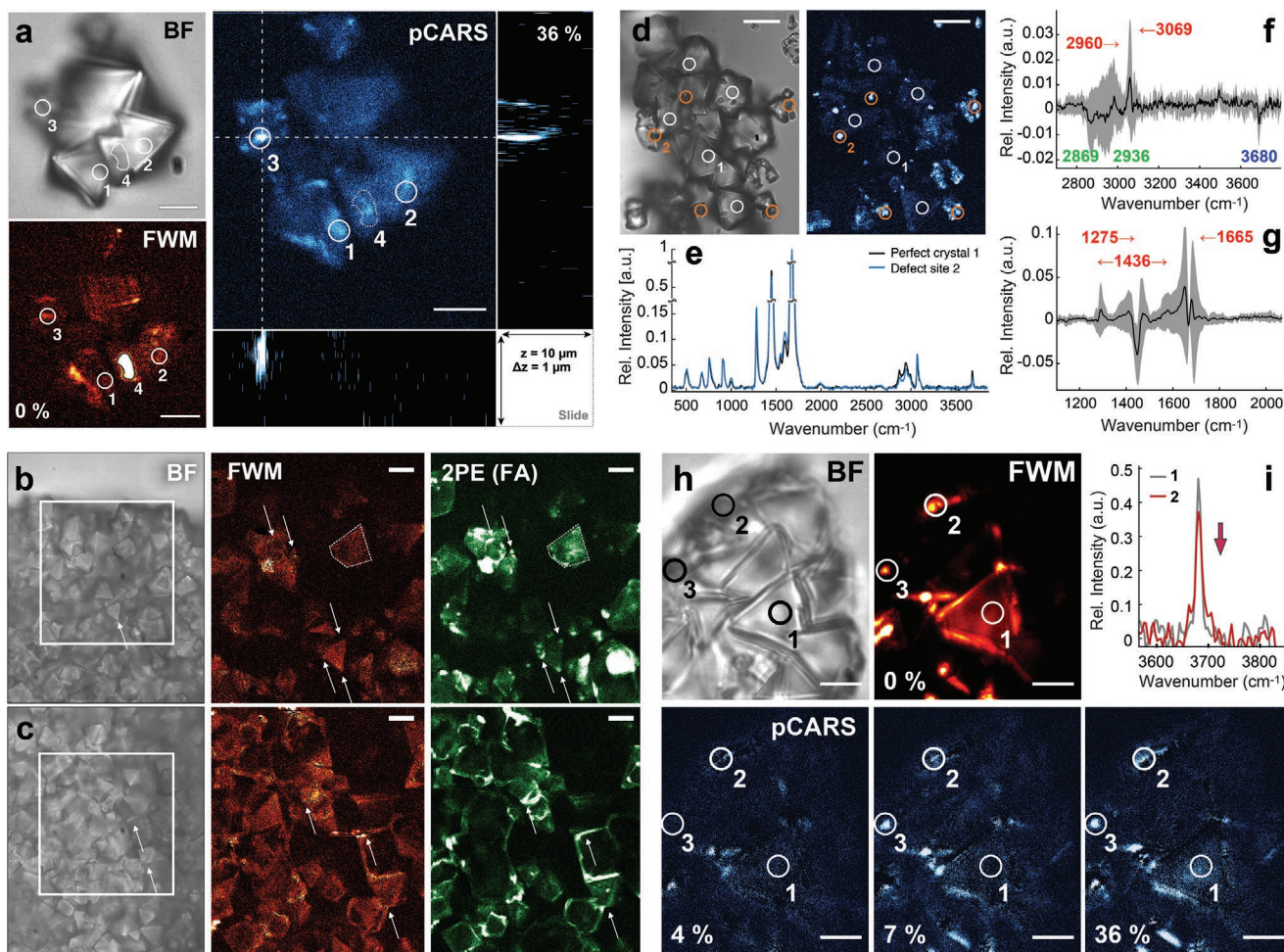


**Figure 5.** Chemical characterization of water clustering sites in MOF-801. a) 3D localization of a confined water cluster in MOF-801 by pCARS at 35.6%RH in comparison to FWM at 0%RH. b,c) Detection of open metal clusters by acid-site assisted polymerization of furfuryl alcohol (FA) in MOF-801 crystals using BF, FWM, and 2PE imaging. Enhanced polymerization is observed at b) edges and tips and c) areas of inter-crystal growth. d–f) Correlative characterization of the chemical environment at areas with enhanced water incorporation by d) pCARS imaging and e–g) spontaneous Raman spectroscopy. Water cluster sites and regular crystals were identified by pCARS imaging at 38.5 %RH (d). e) Raman spectra at positions 1 and 2 that are marked in (d). f–g) Difference spectra between the Raman signature at defect sides and sites of normal crystal growth in the fingerprint region (f) and C-H stretch to water region (g). The mean values (line) and standard deviations (shaded area) represent the average over five locations each. Differences due to missing clusters (blue) and concomitant reduction in residual DMF (green) and uncaging of fumaric acid (red) are marked for the corresponding resonances. Arrows indicate the direction of spectral shift. h) Water distribution at different relative humidities mapped by pCARS imaging in correlation with FWM microscopy at 0%RH and Raman spectroscopy. i) For 0 %RH, the Raman signature at confined water clusters also shows a reduction of the Zr- $\mu_3$ -OH stretch vibration, indicating a smaller degree of metal clusters in MOF-801. Scale bars: 5  $\mu$ m. Abbreviations: bright-field (BF), four-wave mixing (FWM), two-photon excited fluorescence (2PE), polarization-sensitive coherent anti-Stokes Raman scattering (pCARS).

well as at sharp edges of MOF-801 crystals (Figure 5b; arrows). Here, unsaturated metal sites at the interface of three surfaces were freely accessible and featured strong catalytic activity. Enhanced polymerization was further observed at the interface of grain boundaries (Figure 5c; arrows), where different crystals were growing into each other. While the fluorescence assay successfully reported extended defect sites due to missing linkers, the collected material response by FWM imaging hardly co-localized with the signature of polymerized FA molecules, indicating that open metal sites are not the key element responsible for enhanced water incorporation.

Next, we combined pCARS imaging with in situ Raman spectroscopy to directly probe the local chemical environment

around water clusters (Figure 5d–g). First, confined water clusters in MOF-801 were identified via pCARS imaging at 38.5 %RH (marked by orange circles in Figure 5d). Afterward, the sample was dried for half an hour by a nitrogen flow to study the chemical differences without the influence of guest molecules. The chemical composition of MOF-801 in dry state was probed by spontaneous Raman spectroscopy. A comparison (Figure 5d,e) between the spectral signature of a defect site (Position 2) and regular crystal (Position 1) reveals large chemical similarities of the MOF material probed within the confocal volume. Nevertheless, subtle changes in amplitude, that is, in the concentration of different species are apparent. Distinct changes in the fingerprint and water region become

visible in the difference spectrum (between defect sites to crystals; Figure 5f,g). Negative signatures report on species that are more abundant in the regular crystalline material. Figure 5f reveals a decrease in Zr:  $\mu_3$ -OH stretch vibration intensity at  $3680\text{ cm}^{-1}$  and a reduction of the aliphatic C-H stretch vibration between  $2830$  and  $2950\text{ cm}^{-1}$  due to fewer residual DMF molecules. Both findings hint toward missing metal sites that are complexed with residual organic solvent molecules in the regular material. As the vibrational signature of free fumaric acid significantly differs from complexed linker molecules in MOF-801 (Tables S3 and S5, Supporting Information), missing metal sites should cause shifts of the linker-associated resonances. Indeed, we observe a broadening and shift of linker-associated Raman resonances toward the signature of the free fumaric di-anion,<sup>[31]</sup> respectively linker molecule in the fingerprint region (Figure 5g). In particular, the broadening of the symmetric carboxyl stretch vibration at  $1436\text{ cm}^{-1}$  showcases the coexistence of fully-coordinated and partially-coordinated linkers in the studied volume. Our findings indicate that missing clusters defects are majorly responsible for the macropore formation and enhanced water incorporation, which is in line with a missing co-localization with FA polymers that form at metal clusters (Figure 5b,c).

On the other hand, it is unintuitive, as one might expect less binding events of water at missing cluster defects due to its higher affinity for hydrogen bonding to cluster than to carboxylate residues of the linker. As different kinds of defects might contribute at early and later stages of water uptake, we next probed the onset and progression of water adsorption in macropores by pCARS at different humidities. In combination with Raman spectroscopy to identify missing cluster defects and FWM to visualize the material response, the MOSAIC platform can correlate the results and enables in-depth studies of the influences of defect types on water uptake (Figure 5h,i). As expected, FWM shows a heterogeneous material response with strong signals at interfaces and edges (Figure 5h) and highly located defect sites. pCARS reveals already at  $3.9\%$  RH, an overall broad uniform increase of water uptake mixed with confined areas that show an enhanced amount of water. While spontaneous Raman spectroscopy could confirm a reduced availability of metal centers at these sites (Figure 5i), pCARS imaging clearly shows a heterogeneous uptake of water with increasing exposure to humid air: we observed a gradual increase of water uptake, for example, at position 2, while water uptake at position 3 shows an almost stepwise response – which underlines, again, the heterogeneous chemical surrounding of each water cluster.

Overall, our findings give strong evidence that primarily missing metal clusters are responsible for extended defects, which provide additional bindings sites for water. Water can accumulate in the macro-pores created by the initial defects, which consecutively act as seeds for droplet formation and, hence, locally restricted compartments with high water content. Moreover, this example highlights the capability of the developed approach: while each of the applied spectroscopic techniques provides selective insights, MOSAIC allows for combining them in a full picture, in which macropores can be localized, chemically characterized, and water uptake monitored in situ in a spatially resolved manner.

### 3. Conclusion

We presented a dedicated, correlative optical imaging approach combining nonlinear microscopy and spectroscopy to resolve hitherto unexplored property relations of MOF crystals at the single-particle level. Our method addresses the gap of material characterization between the bulk and the unit-cell regime, allowing for studying heterogeneity in properties and their interplay across crystals and within a single crystal. The developed MOSAIC approach allows to study the physical and chemical variance of MOF particles in a label-free manner as shown for UiO-67, to answer how particle composition and morphology affect material properties. To demonstrate this fundamental connection, we explored the orthogonal nature of FWM and degradation-induced chemiluminescence in MIL-88A crystals and could reveal an unexpected correlation between optical properties of the material and their morphology. In a second example, we investigated the chemical nature of extended defects in MOF-801 and showed by a correlative study in situ that heterogeneities in intrinsic properties such as defects in MOF-801 affect the host–guest interaction of the material. These two examples highlight the large versatility of the developed multimodal system, which is easily applicable to study further MOF systems and their heterogeneity with respect to host–guest interaction, multivariance in composition or defects combining information of separate methodologies in situ. Since the interplay of intrinsic and extrinsic properties determines the final performance of the synthesized material, we anticipate that the MOSAIC analysis giving direct access will turn into an important tool for material characterization.

### 4. Experimental Section

**Sample Preparation:** Unlabeled UiO-67 crystals were synthesized from Zirconium(IV) chloride, biphenyl-4,4'-dicarboxylic acid, and benzoic acid following the procedure by Ko et al.<sup>[32]</sup> Labeling of UiO-67 crystals with RBTC by linker exchange followed the protocol by Schrimpf et al.<sup>[10]</sup> Both particle types were evacuated after synthesis and stored in powder form. Crystalline MIL-88A particles as differently sized needles and pyramidal particles were synthesized from Iron(III) chloride hexahydrate and fumaric acid following the optimized procedures described in Hirschle et al.<sup>[22]</sup> They were stored in ethanol or DMF. A detailed description of the synthesis and sample preparation is given in Note S2, Supporting Information.

**Multimodal Nonlinear Scanning Microscope:** Images and spectra were taken on a home-built, confocal laser scanning microscope (Note S1, Supporting Information) equipped with three light sources: two CW lasers at  $532$  and  $633\text{ nm}$  as well as a fiber-based, dual-color femtosecond laser system (FemtoFiber dichro bioMP, Toptica Photonics, Germany) with two synchronized pulse trains at  $80\text{ MHz}$ . It provides laser pulses with  $\approx 180\text{ fs}$  pulse duration and  $1\text{ W}$  output power at  $774\text{ nm}$ . The second fs-laser has a central wavelength of  $1053\text{ nm}$ , an output power of  $1.5\text{ W}$ , and a transform-limited pulse duration of  $\approx 135\text{ fs}$ . The unmodified laser pulses at  $774$  and  $1053\text{ nm}$  serve for 2PE, SHG, and SFG imaging. For FWM and CARS microscopy, laser pulses at  $774\text{ nm}$  are chosen as pump pulses. To coherently excite molecular vibrations in MOFs, the authors employed the  $1053\text{ nm}$  excitation to derive a spectrally broad probe beam by super-continuum generation within a photonic crystal fiber (PCF, NL-1050-Zero-2, NKT Photonics; Note S1, Supporting Information) with spectral components between  $770$  and  $1100\text{ nm}$ . The available supercontinuum was temporally stretched afterward using an SF6 glass rod for spectral focusing. The spectral resolution could be tuned between  $15$  and  $25\text{ cm}^{-1}$  depending on the added chirp. To address the full spectrum of MOF particles, the temporal delay between both laser pulses

was adjusted. The excitation power as well as the linear polarization at 774 nm (tuned for pCARS) were controlled by a half-wave plate in combination with a linear polarizer. The diameter of all exciting lasers was fourfold expanded to overfill the objective of the confocal microscope.

The CW laser lines were superimposed with the designed NIR laser pulses and coupled into the inverted scanning microscope by dichroic mirrors before focusing onto the sample with a water immersion objective (Plan APO VC 60×, 1.2 NA; Nikon). For widefield imaging, the authors used a mercury lamp in combination with an sCMOS camera. Surface scans were performed by using an XYZ-piezo stage with a 200 × 200 × 200 μm travel range. Excitation and detection paths were decoupled via dichroic beam splitters depending on the chosen imaging modalities. The induced signals based on SHG, SFG, FWM, pCARS, and fluorescence in the sample were collected by the same objective, focused onto a 50 μm pinhole and spectrally separated. The authors used an additional notch filter to block the pump wavelength during nonlinear imaging. After suited filtering, the detected light was focused on APDs (Count Blue / Count Red; LaserComponents) for the blue (<620 nm) and red-shifted spectral region, respectively. The detector signal was registered by a dual-channel TCSPC card. The data was recorded using custom software written in Labview 2018 (National Instruments) and C# (VisualStudio 2010, Microsoft). The software employs an FPGA to synchronize the recording, the XYZ scanning via analog output signal, and the TCSPC card via digital TTL trigger. The pulsed signal of the laser (80 MHz) serves as a master clock and is used to trigger the TCSPC card detection intervals. Confocal data was extracted for further analysis using the software framework PAM.<sup>[33]</sup> It was further processed using Fiji<sup>[34]</sup> and Matlab 2018b (The MathWorks, Inc; Natick, MA, USA).

**Nonlinear Imaging:** The excitation power for SHF and SFG imaging amounted up to 20 mW for both channels. FWM and pCARS images of UiO-67 and MOF-801 were recorded with 11.2 mW for the probe pulses and 22.8 mW for the pump pulse, if not stated otherwise. FWM imaging of MIL-88A was performed with  $I_{\text{probe}} = 0.1$  mW and  $I_{\text{pump}} = 1.9$  mW or  $I_{\text{pump}} = 3.0$  mW. For labeled samples, the excitation power was set to 9.9 μW for one-photon excitation at 532 nm, and 2.7 mW for two-photon excitation at 774 nm at the microscope backport. For a good SNR, count rates were always kept between 150 and 400 kHz at an acquisition time per pixel of 180 μs. All images were averaged over three to four frames. For MIL-88A needles, 60 × 60 μm<sup>2</sup> areas with 120 nm pixel-size were chosen as standard parameters (if not specified otherwise). UiO-67 particles were recorded with a pixel size of 160 nm over an area of 500 by 500 pixels (80 μm total image size). MOF-801 crystal clusters were imaged over 50 × 50 μm<sup>2</sup> areas with a pixel size of 100 nm. Single MOF-801 crystals were imaged over 20 × 20 μm<sup>2</sup> areas with a pixel size of 40 nm and averaged over ten frames in z with a step size of 0.5 μm if not stated otherwise.

## Supporting Information

Supporting Information is available from the Wiley Online Library or from the author.

## Acknowledgements

Funding by the Center for NanoScience Munich (CeNS), the Center for Integrated Protein Science Munich (CiPSM), Nanosystems Initiative Munich (NIM), and the Deutsche Forschungsgemeinschaft (PL 696/4-1; WU 622/4-1; Project-ID 201269156 - SFB1032, B03) is gratefully acknowledged. The authors thank Don C. Lamb and Constantin Hoch for support and access to laboratory facilities.

Open access funding enabled and organized by Projekt DEAL.

## Conflict of Interest

The authors declare no conflict of interest.

## Author Contributions

E.P. and S.W. conceived the research. E.P. supervised the project. A.F., P.H., O.Y., S.W., and E.P. designed the experiments. Synthesis and characterization of MOF particles was carried out by P.H., H.W., and Z.J. under the supervision of S.W. and O.Y., respectively. P.H. carried out SEM and XRD experiments. A.F. set up and developed the multimodal system for spectroscopy and imaging with the support from P.M. and carried out the correlative imaging and spectroscopy measurements under the supervision from E.P. A.F., P.H., P.M., and I.Z. performed experiments. A.F., P.H., P.M., S.W., and E.P. analyzed the data. E.P. and A.F. conducted the statistical analysis. E.P. and A.F. designed the figures. A.F., Z.J., S.W., and E.P. wrote the manuscript. All authors approved the final version of the manuscript.

## Data Availability Statement

The data that support the findings of this study are available from the corresponding author upon reasonable request.

## Keywords

heterogeneity, metal–organic framework crystals, nonlinear imaging, particle level, spectroscopy

Received: June 13, 2021

Revised: September 3, 2021

Published online: November 21, 2021

- [1] a) M. Rivera-Torrente, L. D. B. Mandemaker, M. Filez, G. Delen, B. Seoane, F. Meirer, B. M. Weckhuysen, *Chem. Soc. Rev.* **2020**, 49, 6694; b) V. Bon, E. Brunner, A. Pöpl, S. Kaskel, *Adv. Funct. Mater.* **2020**, 30, 1907847.
- [2] L. Liu, D. Zhang, Y. Zhu, Y. Han, *Commun. Chem.* **2020**, 3, 99.
- [3] a) C. Wiktor, M. Meledina, S. Turner, O. I. Lebedev, R. A. Fischer, *J. Mater. Chem. A* **2017**, 5, 14969; b) X. Gong, K. Gnanasekaran, Z. Chen, L. Robison, M. C. Wasson, K. C. Bentz, S. M. Cohen, O. K. Farha, N. C. Gianneschi, *J. Am. Chem. Soc.* **2020**, 142, 17224.
- [4] a) J. Hafizovic, M. Bjørgen, U. Olsbye, P. D. C. Dietzel, S. Bordiga, C. Prestipino, C. Lamberti, K. P. Lillerud, *J. Am. Chem. Soc.* **2007**, 129, 3612; b) E. Brunner, M. Rauche, *Chem. Sci.* **2020**, 11, 4297.
- [5] C. Gropp, S. Canossa, S. Wuttke, F. Gándara, Q. Li, L. Gagliardi, O. M. Yaghi, *ACS Cent. Sci.* **2020**, 6, 1255.
- [6] a) H. Furukawa, K. E. Cordova, M. O’Keeffe, O. M. Yaghi, *Science* **2013**, 341, 1230444; b) L. J. Wang, H. Deng, H. Furukawa, F. Gándara, K. E. Cordova, D. Peri, O. M. Yaghi, *Inorg. Chem.* **2014**, 53, 5881; c) P. Li, N. A. Vermeulen, C. D. Malliakas, D. A. Gómez-Gualdrón, A. J. Howarth, B. L. Mehdi, A. Dohnalkova, N. D. Browning, M. O’Keeffe, O. K. Farha, *Science* **2017**, 356, 624; d) L. Feng, J.-L. Li, G. S. Day, X.-L. Lv, H.-C. Zhou, *Chem* **2019**, 5, 1265; e) M. J. Kalmutzki, N. Hanikel, O. M. Yaghi, *Sci. Adv.* **2018**, 4, eaat9180; f) E. Ploetz, A. Zimpel, V. Cauda, D. Bauer, D. C. Lamb, C. Haisch, S. Zahler, A. M. Vollmar, S. Wuttke, H. Engelke, *Adv. Mater.* **2020**, 32, 1907267.
- [7] J. Fonseca, T. Gong, L. Jiao, H.-L. Jiang, *J. Mater. Chem. A* **2021**, 9, 10562.
- [8] E. Ploetz, H. Engelke, U. Lächelt, S. Wuttke, *Adv. Funct. Mater.* **2020**, 30, 1909062.
- [9] a) R. Ameloot, F. Vermoortele, J. Hofkens, F. C. De Schryver, D. E. De Vos, M. B. J. Roeffaers, *Angew. Chem., Int. Ed.* **2013**, 52, 401; b) K. C. Jayachandrababu, D. S. Sholl, S. Nair, *J. Am. Chem. Soc.* **2017**, 139, 5906.

- [10] W. Schrimpf, J. Jiang, Z. Ji, P. Hirschle, D. C. Lamb, O. M. Yaghi, S. Wuttke, *Nat. Commun.* **2018**, *9*, 1647.
- [11] a) Q. Zhang, X. Tian, H. Zhou, J. Wu, Y. Tian, *Materials* **2017**, *10*, 223; b) J. Langer, D. Jimenez de Aberasturi, J. Aizpurua, R. A. Alvarez-Puebla, B. Auguie, J. J. Baumberg, G. C. Bazan, S. E. J. Bell, A. Boisen, A. G. Brolo, J. Choo, D. Ciolla-May, V. Deckert, L. Fabris, K. Faulds, F. J. Garcia de Abajo, R. Goodacre, D. Graham, A. J. Haes, C. L. Haynes, C. Huck, T. Itoh, M. Käll, J. Kneipp, N. A. Kotov, H. Kuang, E. C. Le Ru, H. K. Lee, J.-F. Li, X. Y. Ling, et al., *ACS Nano* **2020**, *14*, 28; c) J. R. Zhou, G. Tian, L. J. Zeng, X. E. Song, X. W. Bian, *Adv. Healthcare Mater.* **2018**, *7*, 1800022; d) A. C. McKinlay, R. E. Morris, P. Horcajada, G. Ferey, R. Gref, P. Couvreur, C. Serre, *Angew. Chem., Int. Ed.* **2010**, *49*, 6260; e) S. Beg, M. Rahman, A. Jain, S. Saini, P. Midoux, C. Pichon, F. J. Ahmad, S. Akhter, *Drug Discovery Today* **2017**, *22*, 625; f) M. B. J. Roeffaers, R. Ameloot, M. Baruah, H. Uji-i, M. Bulut, G. De Cremer, U. Müller, P. A. Jacobs, J. Hofkens, B. F. Sels, D. E. De Vos, *J. Am. Chem. Soc.* **2008**, *130*, 5763; g) A. Kubarev, E. Plessers, M. Roeffaers, in *Nanotechnology in Catalysis: Applications in the Chemical Industry, Energy Development, and Environment Protection*, (Eds: M. V. de Voorde, B. Sels), Wiley-VCH, Weinheim, Germany **2017**, p. 979; h) C. Sprung, B. M. Weckhuysen, *J. Am. Chem. Soc.* **2015**, *137*, 1916.
- [12] N. Al Danaf, W. Schrimpf, P. Hirschle, D. C. Lamb, Z. Ji, S. Wuttke, *J. Am. Chem. Soc.* **2021**, *143*, 10541.
- [13] a) X. Cheng, J. Yao, H. Zhang, X. Wang, J. Bai, *J. Alloys Compd.* **2021**, *855*, 157433; b) L. R. Mingabudinova, V. V. Vinogradov, V. A. Milichko, E. Hey-Hawkins, A. V. Vinogradov, *Chem. Soc. Rev.* **2016**, *45*, 5408; c) R. Medishetty, L. Nemeč, V. Nalla, S. Henke, M. Samoć, K. Reuter, R. A. Fischer, *Angew. Chem., Int. Ed.* **2017**, *56*, 14743; d) R. Medishetty, J. K. Zareba, D. Mayer, M. Samoć, R. A. Fischer, *Chem. Soc. Rev.* **2017**, *46*, 4976; e) R.-J. Niu, W.-F. Zhou, Y. Liu, J.-Y. Yang, W.-H. Zhang, J.-P. Lang, D. J. Young, *Chem. Commun.* **2019**, *55*, 4873; f) S. Van Cleuvenbergen, I. Stassen, E. Gobechiya, Y. Zhang, K. Markey, D. E. De Vos, C. Kirschhock, B. Champagne, T. Verbiest, M. A. van der Veen, *Chem. Mater.* **2016**, *28*, 3203.
- [14] M. Wolf, K. Hirai, S. Toyouchi, E. Fron, W. Peeters, S. De Feyter, H. Uji-i, *Chem. Commun.* **2020**, *56*, 13331.
- [15] a) B. M. Weckhuysen, *Angew. Chem., Int. Ed.* **2009**, *48*, 4910; b) S. Bordiga, C. Lamberti, F. Bonino, A. Travert, F. Thibault-Starzyk, *Chem. Soc. Rev.* **2015**, *44*, 7262; c) D. Tzoulaki, L. Heinke, H. Lim, J. Li, D. Olson, J. Caro, R. Krishna, C. Chmelik, J. Kärger, *Angew. Chem., Int. Ed.* **2009**, *48*, 3525; d) F. Hibbe, C. Chmelik, L. Heinke, S. Pramanik, J. Li, D. M. Ruthven, D. Tzoulaki, J. Kärger, *J. Am. Chem. Soc.* **2011**, *133*, 2804; e) A. Ghosh, P. Mukherjee, S. Deb, R. Bhargava, *J. Phys. Chem. Lett.* **2017**, *8*, 5325; f) M. Rivera-Torrente, M. Filez, C. Schneider, E. C. van der Feltz, K. Wolkersdörfer, D. H. Taffa, M. Wark, R. A. Fischer, B. M. Weckhuysen, *Phys. Chem. Chem. Phys.* **2019**, *21*, 25678; g) K.-L. Liu, A. V. Kubarev, J. Van Loon, H. Uji-i, D. E. De Vos, J. Hofkens, M. B. J. Roeffaers, *ACS Nano* **2014**, *8*, 12650; h) K. F. Domke, T. A. Riemer, G. Rago, A. N. Parvulescu, P. C. A. Bruijninx, A. Enejder, B. M. Weckhuysen, M. Bonn, *J. Am. Chem. Soc.* **2012**, *134*, 1124; i) C. Hess, *Chem. Soc. Rev.* **2021**, *50*, 3519; j) I. Strauss, A. Mundstock, M. Treger, K. Lange, S. Hwang, C. Chmelik, P. Rusch, N. C. Bigall, T. Pichler, H. Shiozawa, J. Caro, *ACS Appl. Mater. Interfaces* **2019**, *11*, 14175; k) A. M. Katzenmeyer, J. Canivet, G. Holland, D. Farrusseng, A. Centrone, *Angew. Chem., Int. Ed.* **2014**, *53*, 2852; l) A. M. Katzenmeyer, V. Aksyuk, A. Centrone, *Anal. Chem.* **2013**, *85*, 1972; m) G. Delen, M. Monai, F. Meirer, B. M. Weckhuysen, *Angew. Chem., Int. Ed.* **2021**, *60*, 1620.
- [16] a) C. E. Harvey, E. M. van Schroyen Lantman, A. J. G. Mank, B. M. Weckhuysen, *Chem. Commun.* **2012**, *48*, 1742; b) A. I. Gómez-Varela, D. R. Stamov, A. Miranda, R. Alves, C. Barata-Antunes, D. Dambournet, D. G. Drubin, S. Paiva, P. A. A. De Beule, *Sci. Rep.* **2020**, *10*, 1122; c) P. Bondia, S. Casado, C. Flors, *Methods Mol. Biol.* **2017**, *1663*, 105; d) H. Abramczyk, A. Imiela, B. Brozek-Pluska, M. Kopec, *Nanomedicine* **2019**, *14*, 1873; e) W. R. Adams, B. Mehl, E. Lieser, M. Wang, S. Patton, G. A. Throckmorton, J. L. Jenkins, J. B. Ford, R. Gautam, J. Brooker, E. D. Jansen, A. Mahadevan-Jansen, *Sci. Rep.* **2021**, *11*, 8067.
- [17] J.-X. Cheng, L. D. Book, X. S. Xie, *Opt. Lett.* **2001**, *26*, 1341.
- [18] M. Mohseni, C. Polzer, T. Hellerer, *Opt. Express* **2018**, *26*, 10230.
- [19] a) A. Guo, M. Durymanov, A. Permyakova, S. Sene, C. Serre, J. Reineke, *Pharm. Res.* **2019**, *36*, 53; b) P. Horcajada, T. Chalati, C. Serre, B. Gillet, C. Sebrie, T. Baati, J. F. Eubank, D. Heurtaux, P. Clayette, C. Kreuz, J. S. Chang, Y. K. Hwang, V. Marsaud, P. N. Bories, L. Cynober, S. Gil, G. Ferey, P. Couvreur, R. Gref, *Nat. Mater.* **2010**, *9*, 172; c) S. Rojas, A. Arenas-Vivo, P. Horcajada, *Coord. Chem. Rev.* **2019**, *388*, 202.
- [20] H. Tan, G. Tang, Z. Wang, Q. Li, J. Gao, S. Wu, *Anal. Chim. Acta* **2016**, *940*, 136.
- [21] S. Gholizadeh Khasevani, M. R. Gholami, *Inorg. Chem. Commun.* **2019**, *102*, 221.
- [22] P. Hirschle, C. Hirschle, K. Böll, M. Döblinger, M. Höhn, J. M. Tuffnell, C. W. Ashling, D. A. Keen, T. D. Bennett, J. O. Rädler, E. Wagner, M. Peller, U. Lächelt, S. Wuttke, *Chem. Mater.* **2020**, *32*, 2253.
- [23] a) L. Lewin, *J. Inst. Electr. Eng., Part 3* **1947**, *94*, 65; b) X. Fan, W. Zheng, D. J. Singh, *Light Sci. Appl.* **2014**, *3*, e179; c) B. R. Johnson, *J. Opt. Soc. Am. A* **1993**, *10*, 343.
- [24] a) L. Rayleigh, *London Edinburgh Dublin Philos. Mag. J. Sci.* **1899**, *47*, 375; b) G. Mie, *Ann. Phys.* **1908**, *330*, 377; c) L. Lorenz, *Eur. Phys. J H* **1890**, *44*, 135; d) C. F. Bohren, D. R. Huffman, *Absorption and Scattering of Light by Small Particles*, Wiley-VCH, Weinheim, Germany **1998**, p. 57.
- [25] A. I. Kuznetsov, A. E. Miroshnichenko, M. L. Brongersma, Y. S. Kivshar, B. Luk'yanchuk, *Science* **2016**, *354*, 846.
- [26] N. K. Kulachenkov, S. Bruyere, S. A. Sapchenko, Y. A. Mezenov, D. Sun, A. A. Krasilin, A. Nominé, J. Ghanbaja, T. Belmonte, V. P. Fedin, E. A. Pidko, V. A. Milichko, *Adv. Funct. Mater.* **2019**, *30*, 1908292.
- [27] a) H. Kim, S. Yang, S. R. Rao, S. Narayanan, E. A. Kapustin, H. Furukawa, A. S. Umans, O. M. Yaghi, E. N. Wang, *Science* **2017**, *356*, 430; b) F. Fathieh, M. J. Kalmutzki, E. A. Kapustin, P. J. Waller, J. Yang, O. M. Yaghi, *Sci. Adv.* **2018**, *4*, eaat3198.
- [28] H. Furukawa, F. Gandara, Y. B. Zhang, J. Jiang, W. L. Queen, M. R. Hudson, O. M. Yaghi, *J. Am. Chem. Soc.* **2014**, *136*, 4369.
- [29] A. K. Cheetham, T. D. Bennett, F.-X. Coudert, A. L. Goodwin, *Dalton Trans.* **2016**, *45*, 4113.
- [30] M. Choura, N. M. Belgacem, A. Gandini, *Macromolecules* **1996**, *29*, 3839.
- [31] L. Maury, L. Bardet, R. Brunel, R. Vierende, *J. Raman Spectrosc.* **1981**, *11*, 14.
- [32] N. Ko, J. Hong, S. Sung, K. E. Cordova, H. J. Park, J. K. Yang, J. Kim, *Dalton Trans.* **2015**, *44*, 2047.
- [33] W. Schrimpf, A. Barth, J. Hendrix, D. C. Lamb, *Biophys. J.* **2018**, *114*, 1518.
- [34] a) J. Schindelin, I. Arganda-Carreras, E. Frise, V. Kaynig, M. Longair, T. Pietzsch, S. Preibisch, C. Rueden, S. Saalfeld, B. Schmid, J.-Y. Tinevez, D. J. White, V. Hartenstein, K. Eliceiri, P. Tomancak, A. Cardona, *Nat. Methods* **2012**, *9*, 676; b) C. T. Rueden, J. Schindelin, M. C. Hiner, B. E. DeZonia, A. E. Walter, E. T. Arena, K. W. Eliceiri, *BMC Bioinformatics* **2017**, *18*, 529.